Progress In Electromagnetics Research Letters, Vol. 130, 44–51, 2026

PIER Letters

(Received 4 March 2026, Accepted 2 April 2026, Scheduled 30 April 2026)

Design of a Single Layer Substrate and Via-Free Transmit-Reflect Array Antenna Based on Metasurface

Xinwei Chen, Xinmiao Zhao, Jinrong Su, Guorui Han, Runbo Ma, and Li Li*

ABSTRACT: In this study, a single-layer substrate and via-free transmit-reflect-array antenna based on a metasurface is proposed. The array antenna comprises transmissive and reflective unit cells arranged alternately in sequence. To achieve a 360° phase coverage, two sets of antisymmetric U-shaped lines were etched on the top and bottom layers of the substrate to form the transmissive unit cells, and multi-layer stacking and vias are avoided. Moreover, by adjusting the lengths of a split-ring structure with phase delay lines for reflective unit cells, a 360° phase coverage was achieved. The measurement results demonstrated that the antenna simultaneously generates a reflective focused beam with a peak gain of 20.8 dBi and a transmissive $+1$-mode OAM vortex beam with a peak gain of 20 dBi and a mode purity of 90 % at 17 GHz.

1. INTRODUCTION

With the rapid development of modern communication systems, the requirements for antenna performance are becoming increasingly stringent. Metasurfaces exhibit tremendous application potential in antennas owing to their unique electromagnetic properties [1–3]. The phase [4], amplitude [5], polarization [6], and frequency [7, 8] of electromagnetic waves can be flexibly manipulated. Modern metamaterials have made tremendous strides in leveraging structural asymmetry to achieve multifunctional, multitasking optical, and electromagnetic control. Specifically, recent studies have successfully utilized the Photonic Spin Hall Effect (PSHE) in asymmetric Janus metastructures to achieve multi-scale and multitasking sensing in the terahertz regime [9]. Furthermore, structural asymmetry has been widely employed to design high-sensitivity multitasking non-reciprocal sensors for biological and angle sensing [10], as well as short-wave infrared Janus metastructures capable of wide-range pressure detection and high-resolution biosensing [11].

Currently, most conventional metasurfaces operate solely as transmitarray or reflectarray antennas. Furthermore, transmitarray antennas generally consist of multilayer structures to achieve satisfactory performance, resulting in an elevated antenna profile [12, 13]; reflectarray antennas are constrained in beam steering owing to the feed antenna placed in front of the reflectarray, which causes blockage of the reflected wavefronts [14]. Both types of antennas are confined to a half-space radiation domain, resulting in a relatively narrow coverage scope.

In recent years, transmit-reflect metasurfaces have become a research hotspot. To achieve full 360° phase coverage, most of these metasurfaces are designed with complex multilayer architectures [15, 16] to accumulate the spatial phase, resulting in a large overall size and high profile. For example, the non-interleaved bidirectional metasurface achieves full-space energy partitioning using seven metallic layers and six dielectric substrates; while its control capability is enhanced, the fabrication difficulty is significantly greater than that of single-layer dielectric structures [17]. The bidirectional transmitarray based on sparse arrays requires stacking three dielectric substrates, resulting in an overall thickness of $0.452\lambda_0$, and interlayer misalignment errors may introduce extrinsic losses [18]. The broadband, high-efficiency, and ultrathin metasurface proposed by Wang et al. [19] realizes the independent modulation of transmissive and reflective amplitudes and phases via stacking multilayer dielectric and metallic layers. To decrease the profile of the metasurface, integrated metallic vias have been adopted in single-layer structures to achieve a low profile [20, 21]. The metal vias are incorporated into a single-layer substrate to realize full-space beam integration; however, the coupling between the vias and metallic structures elevates the cross-polarization ratio (XPR) to -17.4 dB and introduces a loss of approximately 1.2 dB.

Since most existing metasurface structures are multilayer stacking or metallic vias, this paper designs a metasurface capable of generating transmissive and reflective beams without multilayer stacking or metallic vias. The transmissive unit cell adopts an antisymmetric Huygens source structure, and the reflective unit cell is a split-ring resonator loaded with phase delay lines. Two types of unit cells are alternately arranged in odd and even columns to complete the phase compensation and construct a single-layer integrated array. The designed transmit-reflect-array antenna generates a high-gain focused beam in the reflective mode and a $+1$-mode OAM vortex beam in the transmissive mode.

2. DESIGN OF TRANSMISSIVE UNIT CELL AND REFLECTIVE UNIT CELL

The proposed transmissive unit cell is illustrated in Figure 1. Based on Huygens' principle, two mutually antisymmetric U-

---

* Corresponding author: Li Li (lili@sxu.edu.cn).

doi:10.2528/PIERL26030411

Published by THE ELECTROMAGNETIC ACADEMY

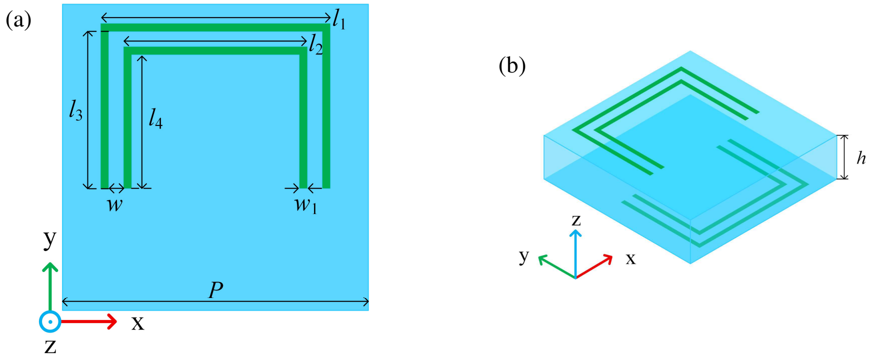

FIGURE 1. Structure of the transmissive unit cell. (a) Top layer. (b) Three-dimensional view.

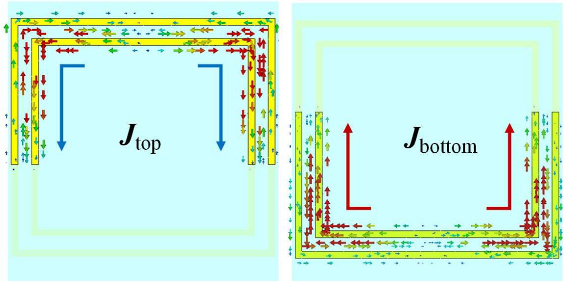

FIGURE 2. The surface current distributions of the transmissive unit at 17 GHz.

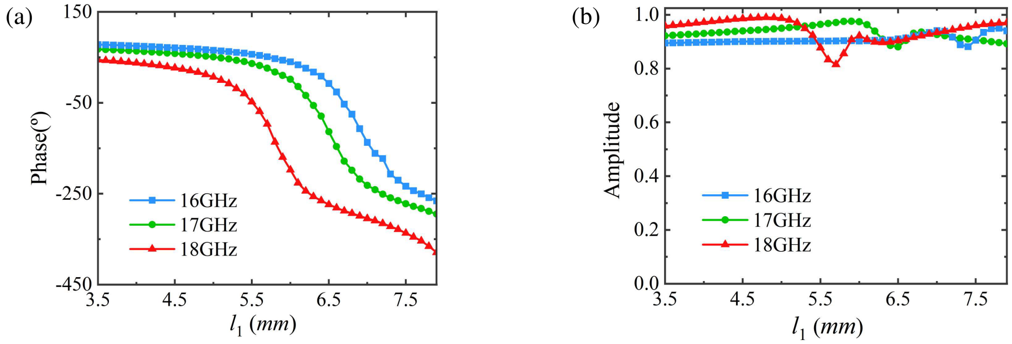

FIGURE 3. The transmissive phase and amplitude. (a) Phase. (b) Amplitude.

shaped lines were etched on the top and bottom surfaces of an F4B dielectric substrate ($\varepsilon_r = 2.2$, $\tan\delta = 0.001$ and $h = 2.5\,\mathrm{mm}$). Figures 1(a) and (b) depict the top and 3D views of the structure, respectively. The geometric parameters were defined as follows: $P = 8\,\mathrm{mm}$, $w = 0.5\,\mathrm{mm}$, $w_1 = 0.2\,\mathrm{mm}$, $l_3 = 4.1\,\mathrm{mm}$,$l_4 = 3.5\,\mathrm{mm}$, $l_2 = l_1$-1.2 mm. By changing l_1 and l_2, the transmissive phase can be precisely controlled.

Figure 2 illustrates the surface current distributions of the transmissive unit at 17 GHz, Obviously, the surface electric currents $\mathbf{J}_{\mathrm{top}}$ on the top corner-shaped ring and $\mathbf{J}_{\mathrm{bottom}}$ on the bottom strip-type ring are generated and flow in opposite directions, thereby forming a current loop with the F4B substrate and then inducing an orthogonal magnetic current. Therefore, the electromagnetic (EM) waves irradiated on the Huygens' metasurface can be efficiently tailored by simultaneously inducing the orthogonal electric and magnetic currents and the Huygens' resonance stimulated by their interaction.

The effect of the transmissive unit cell on the magnitude and phase was investigated. Figure 3 shows the variation in the transmissive phase and amplitude with l_1 over the 16–18 GHz under y-polarized incidence wave. As illustrated in Figure 3(a), as l_1 increases from 3.5 mm to 7.5 mm (with l_2 varying from 2.3 mm to 6.3 mm accordingly), the transmissive phase achieves a full 360° phase coverage. As shown in Figure 3(b), throughout the tuning range of l_1, the transmissive amplitude remains stable at approximately 0.9 above 16 and 17 GHz and slightly less than 0.8 at 18 GHz.

Figure 4 shows the proposed reflective unit cell, which comprises a top metallic layer and a metallic ground plane separated by an F4B dielectric substrate ($\varepsilon_r = 2.2$, $\tan\delta = 0.001$ and $h = 2.5\,\mathrm{mm}$). The top metallic layer is a split-ring resonator (SRR) loaded with symmetric phase delay lines. By tuning the φ_1 of the phase delay line, a reflective phase of 360° can be achieved. The geometric parameters are defined as follows:

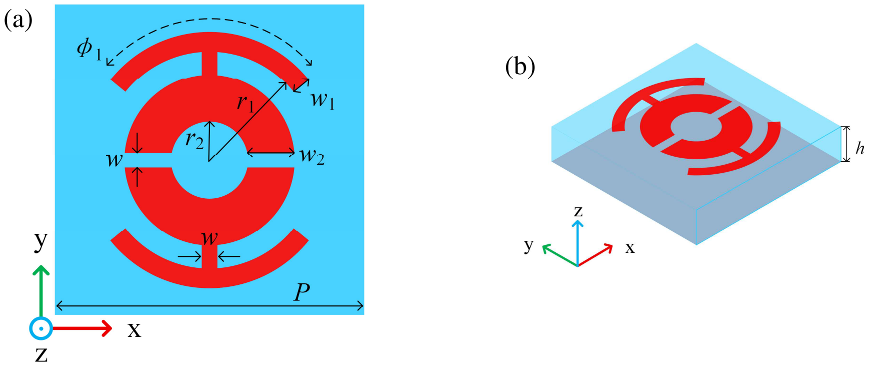

FIGURE 4. Structure of the reflective unit cell. (a) Top layer. (b) Three-dimensional view.

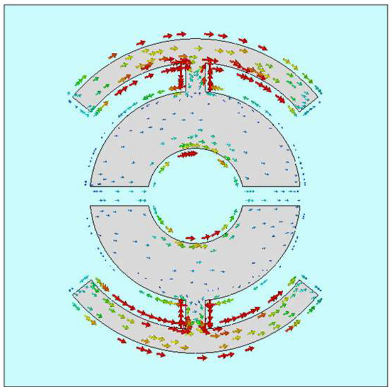

FIGURE 5. The surface current distributions of the reflective unit at 17 GHz.

$P = 8$ mm, $w = 0.4$ mm, $w_1 = 0.5$ mm, $w_2 = 1.2$ mm, $r_1 = 2.8$ mm, $r_2 = 1$ mm.

Figure 5 shows the surface current distributions of the reflective unit at 17 GHz. The electric field energy is mainly concentrated in phase delay lines. Therefore, phase control can be realized by adjusting the length of the symmetric phase delay lines loaded on the split ring. The effects of different phase delay lines on the magnitude and phase were investigated. Figure 6 shows the reflective phase and amplitude at different φ_1 values over the 16–18 GHz under y-polarized incidence wave. As φ_1 increases from 5° to 175° (in 10° increments), the reflective phase exhibits a decrease with a 400° phase coverage. The reflective amplitude remains stable at approximately 1.

As shown in Figure 7, the phase and amplitude of the unit cell are plotted for incident angles of 0°, 15°, and 30°, respectively. It can be observed that the phase shift varies slightly as the incident angle increases from 0° to 30°, indicating that the unit cell exhibits excellent angular stability. Meanwhile, the transmissive amplitude remains above 0.75, and the reflective amplitude is consistently close to 1.

3. DESIGN OF ARRAY ANTENNA

The proposed transmit-reflect-array antenna comprises 26×26 transmissive and reflective unit cells operating at 17 GHz, as shown in Figure 8. These two types of unit cells were alternately arranged in odd and even columns to implement phase compensation. The total size was 208 mm × 208 mm ($11.78\lambda_0 \times 11.78\lambda_0$, where λ_0 denotes the free-space wavelength at 17 GHz). When the transmit-reflect-array is fed by a y-polarized horn feed antenna positioned at $Z = 150$ mm (focal-to-diameter ratio of 0.72), a high-gain focused beam in the reflective mode and a $+1$ mode OAM vortex beam in the transmissive mode are generated, respectively.

The detailed phase compensation procedure is illustrated in Figure 9. Because the wave emitted by the horn is a spherical wave, the compensated focused phase of the metasurface is shown in Figure 9(a), and its formula follows [22]:

$$\varphi_f = k_0 \left(\sqrt{x^2 + y^2 + F^2} - F \right) \tag{1}$$

where k_0 is the wavenumber, which is numerically equal to $2\pi/\lambda_0$, and F is the focal length. Because the reflective and transmissive unit cells are alternately arranged on the metasurface, the overall focal compensation phases are decomposed into reflective and transmissive compensation phases, respectively, as shown in Figs. 9(b)–9(c). Moreover, the vortex phase (with a mode number of $+1$) shown in Figure 9(d) must be superimposed onto the transmissive compensation phases. The vortex phase that generates an orbital angular momentum (OAM) beam with $l = +1$ can be calculated using the following formula, where l is the OAM mode.

$$\varphi_{OAM} = l \cdot \arctan\left(\frac{y}{x}\right) \tag{2}$$

The transmissive OAM phase is shown in Figure 9(e). The superimposed phase distribution of the reflective focused beam and transmissive OAM beam full-space metasurface is shown in Figure 9(f).

As shown in Figs. 10(a)–10(b), the geometric dimension distributions of the unit cells in the even and odd columns are established corresponding to the phase distributions of Figure 9(f). Here, the even-numbered columns are reflective unit cells, whereas the odd-numbered columns are transmissive unit cells.

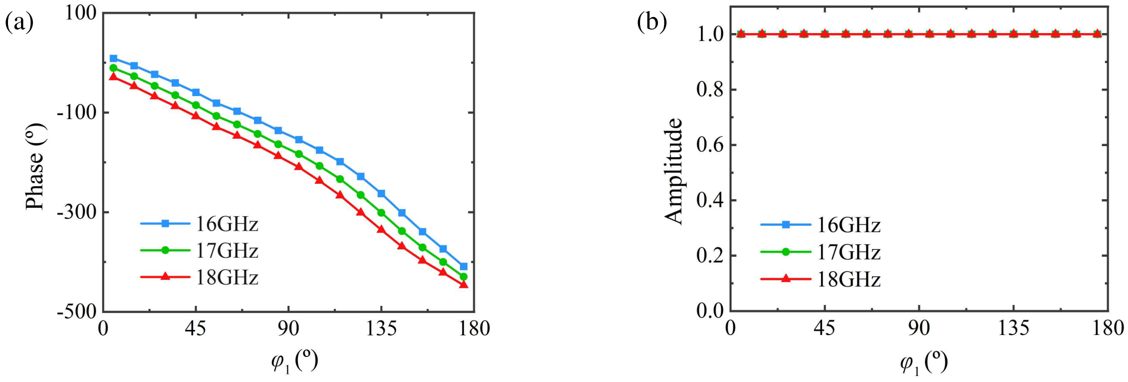

FIGURE 6. Reflective phase and amplitude. (a) Phase. (b) Amplitude.

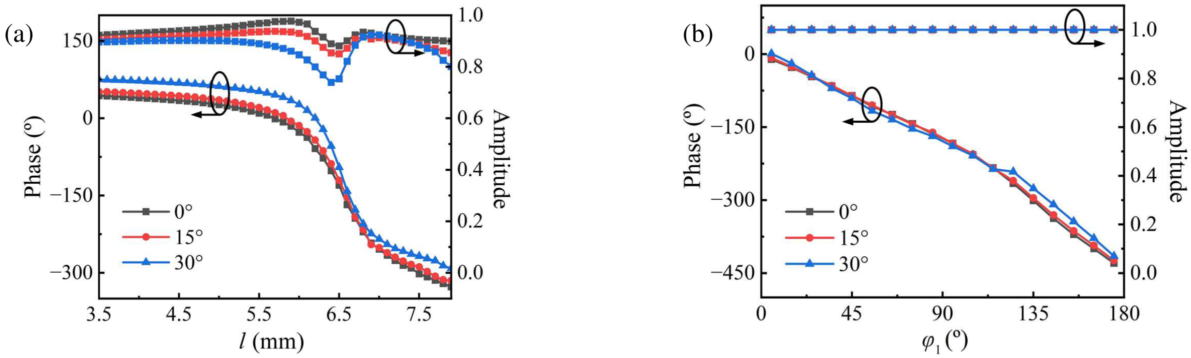

FIGURE 7. The phase and amplitude of the unit cell at different incident angles at 17 GHz. (a) Transmissive unit cell. (b) Reflective unit cell.

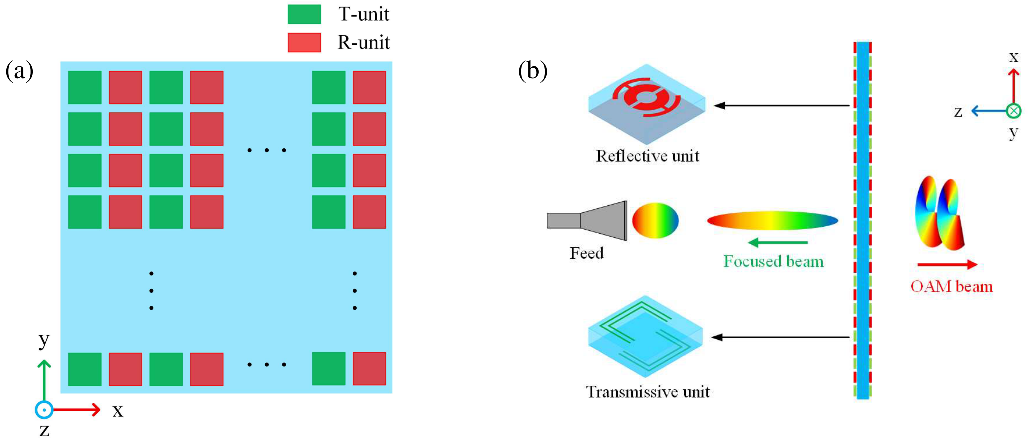

FIGURE 8. The transmit-reflect-array mode and its working schematic diagram. (a) The transmit-reflect-array mode. (b) The working schematic diagram of array.

4. RESULT ANALYSIS

Figure 11 illustrates the radiation characteristics of the metasurface array at 17 GHz. In particular, the designed transmit-reflect-array radiates a focused beam with a peak gain of 21.5 dBi in the reflective half-space and generates an OAM beam with a peak gain of 20.2 dBi in the transmissive half-space.

To characterize the near-field electromagnetic distribution, an observation plane of 208 mm×208 mm was positioned 400 mm below the metasurface along the $+z$-axis. The electric field phase and amplitude distributions of the transmissive OAM beam are shown in Figure 12. At the given frequency, the OAM beam exhibited a donut-shaped electric-field amplitude and a 360° helical electric-field phase. Based on the obtained electric-field phase and amplitude distributions, the mode purity was analyzed using the Fourier transform with the following formula [23]:

$$A_l = \frac{1}{2\pi}\int_0^{2\pi} \psi(\varphi) \mathrm{e}^{-\mathrm{j}l\varphi} d\varphi \qquad (3)$$

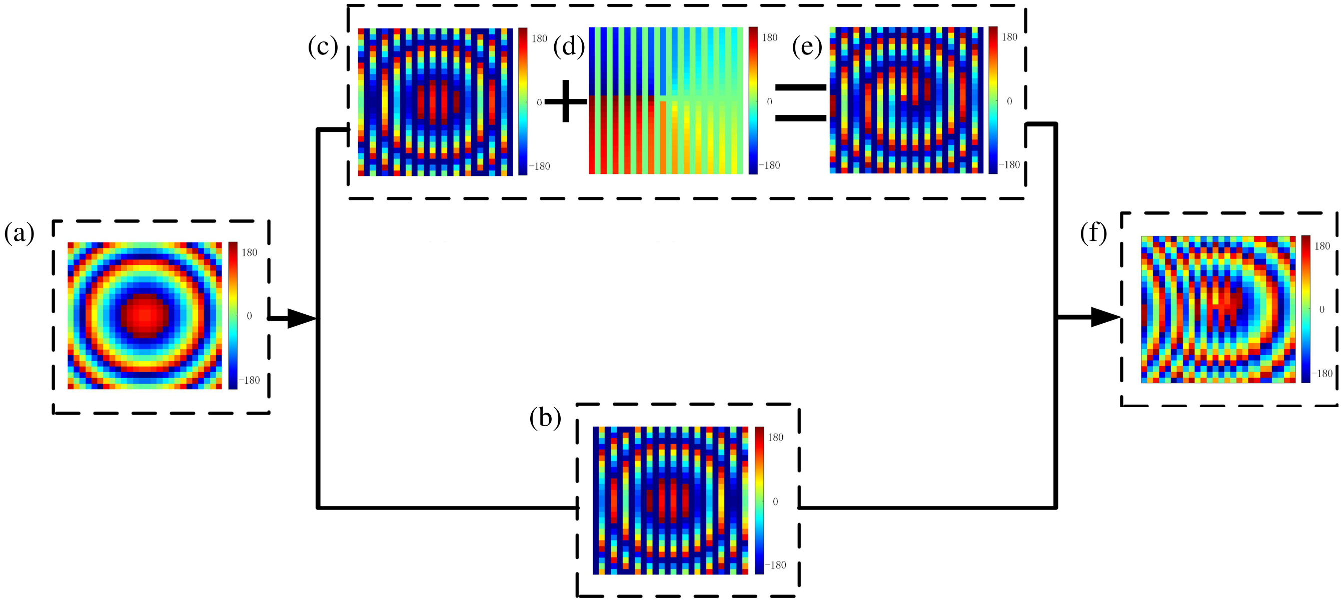

FIGURE 9. Phase compensation process. (a) Focal compensation phase. (b) Reflective compensation phases distribution. (c) Transmissive compensation phases distribution. (d) $l = +1$ vortex phase. (e) Transmissive OAM phase. (f) Overall phase distribution.

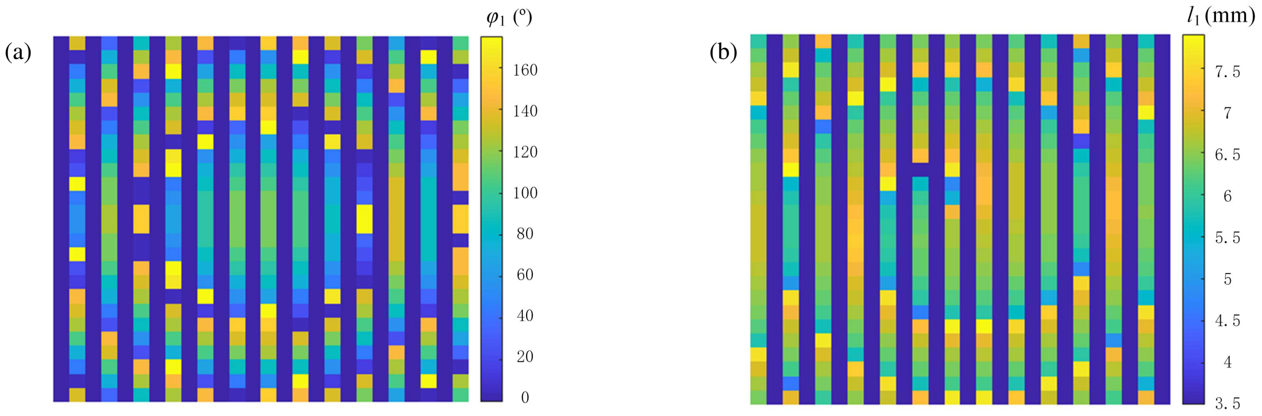

FIGURE 10. Geometric dimension distributions. (a) The size of φ_1 in the reflective unit cells (Even Columns). (b) The size of l_1 in the transmissive unit cells (Odd Columns).

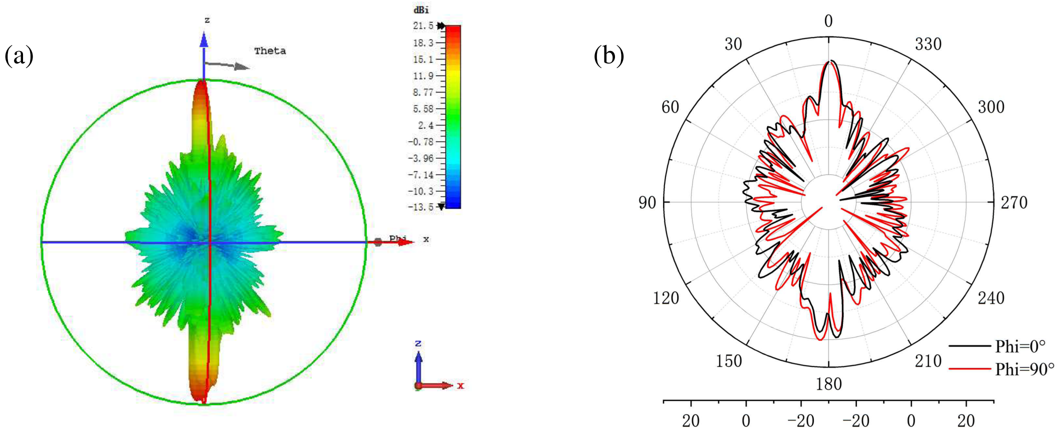

FIGURE 11. Radiation pattern at 17 GHz. (a) 3D Radiation pattern. (b) 2D Radiation pattern.

TABLE 1. Literature comparison.

Ref.	Frequency Range/GHz	Peak gain /dBi	Aperture Efficiency	Size	Thickness	Function	Substrate Layers	Vias
[12]	30	T-23.8	22.1%	$\pi\ (5.25\lambda_0)^2$	$0.18\lambda_0$	T-OAM	4	No
[14]	12	R-20	N	$(12\lambda_0)^2$	$0.12\lambda_0$	R-OAM	1	No
[17]	11.5	T-21.4 R-23.2	T-41.1% R-41.6%	$\pi\ (3.85\lambda_0)^2$	$0.345\lambda_0$	T-Focused R-Focused	6	No
[18]	30	T-21.4 R-24.4	T-7.0% R-14.0%	$(12.5\lambda_0)^2$	$0.45\lambda_0$	T-Focused R-Focused	3	No
[19]	30	N	N	$(16\lambda_0)^2$	$0.1\lambda_0$	T-OAM R-OAM	2	No
[21]	28–32	T-16.4/16.5 R-17.2/17.4	T-4.6% R-5.6%	$(12.48\lambda_0)^2$	$0.12\lambda_0$	R-OAM T-Focused	1	Yes
[23]	26–30	T-30.3 R-30.3	T-45.6% R-45.7%	$\pi\ (7.7\lambda_0)^2$	$0.14\lambda_0$	Focused (T/R)	1	No
[24]	26/38	T-28.32 R-30.61	T-43.1% R-34.2%	$\pi\ (9.24\lambda_0)^2$	$0.19\lambda_0$	Focused (T/R)	1	No
[25]	10	T-25.5 R-25.0	T-15% R-14%	$(14\lambda_0)^2$	$0.067\lambda_0$	Focused (T/R)	1	No
[26]	30	T-22.25 R-20.23	T-17.2% R-11.1%	$(8.8\lambda_0)^2$	N	T-Focused R-Focused	1	No
This Work	17	T-20.0 R-20.8	T-5.7% R-6.9%	$(11.78\lambda_0)^2$	$0.14\lambda_0$	T-OAM R-Focused	1	No

N, None; T, Transmissive; R, Reflective

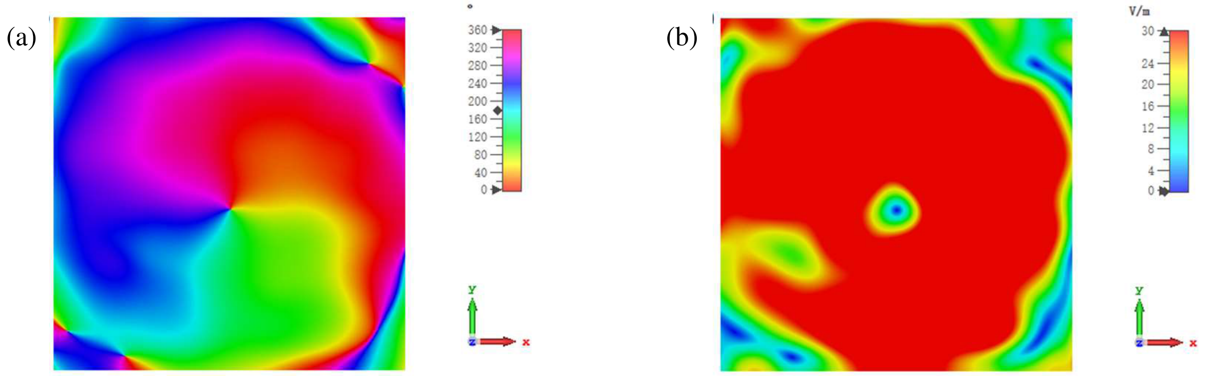

FIGURE 12. Electric field characteristics of the transmissive OAM beam at 17 GHz. (a) Phase distribution. (b) Amplitude distribution.

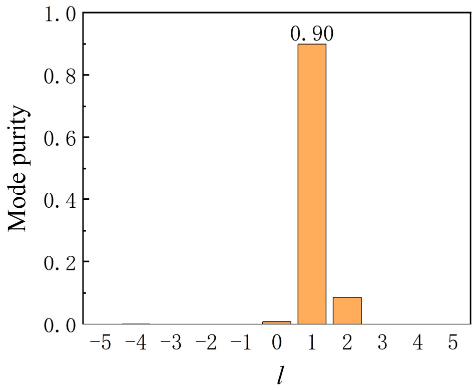

FIGURE 13. Mode purity of the transmissive OAM beam at 17 GHz.

$$\psi(\varphi) = \sum_{1} \mathrm{A}_1 \mathrm{e}^{\mathrm{j}l\varphi} \tag{4}$$

Here, $\psi(\varphi)$ denotes the sampled field function along the circumference centered on the z-axis. The OAM modes with l ranging from -5 to 5 are considered, and the energy weight of mode l is defined as follows:

$$E_l = \frac{A_l}{\sum_{l'=-5}^{5} A_{l'}} \tag{5}$$

The center of the electric field distribution is set as the center of the sampling ring with a radius of 104 mm. A total of 100 sampling points is uniformly distributed along the ring at

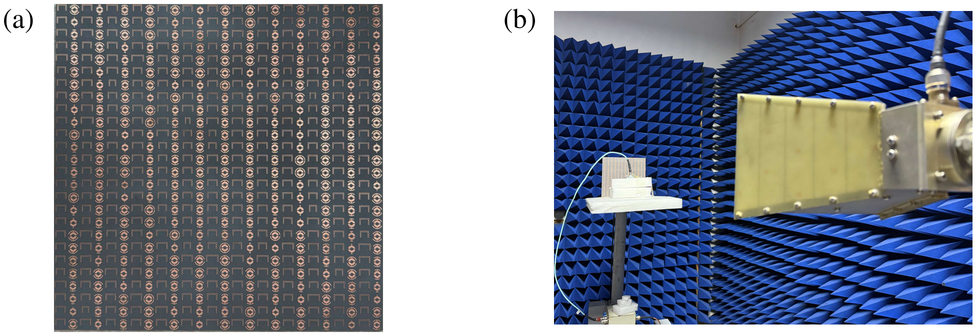

FIGURE 14. The metasurface and measurement environment. (a) The front side of the metasurface. (b) The measurement environment.

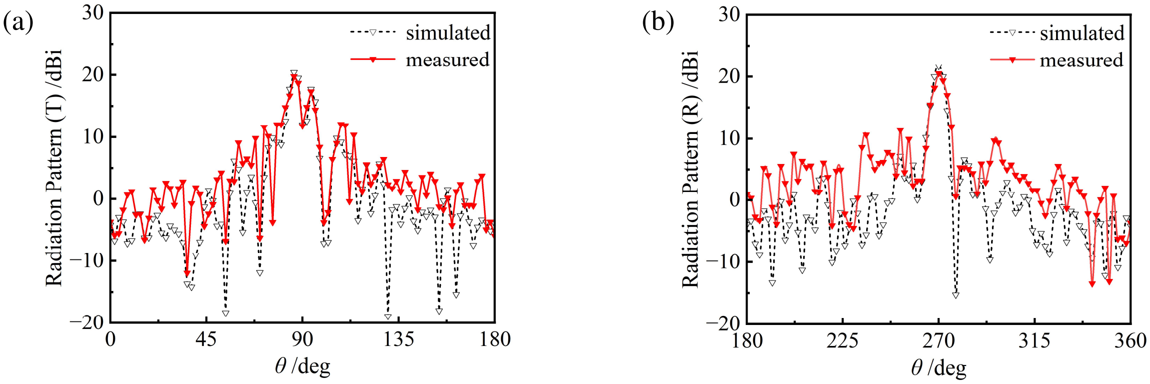

FIGURE 15. The simulated and measured radiation patterns. (a) Transmissive vortex beam. (b) Reflective focused beam.

equal angular intervals to obtain the complex electric field distribution. Through azimuthal Fourier decomposition, the field is decomposed into a superposition of different OAM modes. After normalizing the mode amplitudes, the energy proportion of the dominant mode $l = +1$ is calculated as 90%, corresponding to the mode purity. Figure 13 shows the mode purity of the generated OAM beam.

To verify the feasibility, the designed transmit-reflect-array antenna was fabricated and measured. Figure 14 shows the fabricated array prototype and the measurement environment. The transmit-reflect-array antenna comprised 26 × 26 unit cells, wherein the transmissive units were arranged in the odd columns, and the reflective units were arranged in the even columns. An LB-75-10-C-SF standard gain horn antenna was used for feeding at a distance of 150 mm in front of the metasurface, while the receiving horn was placed 1.5 m in front of the metasurface to receive the electromagnetic wave. The far-field radiation patterns are shown in Figure 15. The measured focused beam with a peak gain of 20.8 dBi in the reflective half-space and an OAM beam with a peak gain of 20 dBi in the transmissive half-space can be observed. Excellent agreement was observed between the measured and simulated data. The slight discrepancies in the gain can be primarily attributed to unstable measurement environments, feed alignment errors, and inaccurate fabrication.

Table 1 presents a comparative analysis of the performance metrics between the designed antenna and those of state-of-the-art antennas. The metasurface proposed in this study can achieve full 360° phase coverage and enables bidirectional radiation using a single-layer substrate without vias. However, the designs [12] and [14] exhibit single-mode operation and unifunctional behavior, failing to achieve full spatial utilization. In contrast, full-space metasurface designs in [17–19, 21] rely on complex structural configurations, and bidirectional radiation is achieved with multi-layered structures or the incorporation of metallic vias. Although the designs reported in [23, 25] can realize both transmission and reflection functions, they cannot achieve the two functions simultaneously. While the design presented in [26] is capable of generating transmissive and reflective beams simultaneously within a single-layer and via-free structure, it can only produce pencil beams, which correspond to distinct application scenarios.

5. CONCLUSION

In this study, a single-layer substrate and a via-free transmit-reflect-array antenna were designed. The transmissive units adopt an antisymmetric Huygens source structure, whereas the reflective units use split-ring resonators loaded with phase delay lines. The alternating arrangement of these two types of units forms the transmit-reflect-array, achieving maximum spatial utilization and bidirectional radiation characteristics. The measured results demonstrate that the antenna can radiate a reflective focused beam with a peak gain of 20.8 dBi and a transmissive +1-mode OAM vortex beam with a peak gain of 20 dBi at 17 GHz.

ACKNOWLEDGEMENT

This work was supported by the Natural Science Foundation of Shanxi Province (202203021211295) and Research Project Supported by Shanxi Scholarship Council of China (2024-017).

REFERENCES

[1] Fan, Y., N.-H. Shen, F. Zhang, Q. Zhao, Z. Wei, P. Zhang, J. Dong, Q. Fu, H. Li, and C. M. Soukoulis, "Photoexcited graphene metasurfaces: Significantly enhanced and tunable magnetic resonances," *ACS Photonics*, Vol. 5, No. 4, 1612–1618, 2018.

[2] Lin, D., P. Fan, E. Hasman, and M. L. Brongersma, "Dielectric gradient metasurface optical elements," *Science*, Vol. 345, No. 6194, 298–302, 2014.

[3] Luo, X., "Subwavelength optical engineering with metasurface waves," *Advanced Optical Materials*, Vol. 6, No. 7, 1701201, 2018.

[4] Hao, H., Z. Cai, B. Li, and P. Tang, "Design of double-layer circular polarization multiplex focusing metasurface lens," *Progress In Electromagnetics Research C*, Vol. 144, 169–180, 2024.

[5] Hao, H., S. Zheng, Y. Tang, and X. Ran, "Broadband transmissive amplitude-and-phase metasurface for vortex beam generation and hologram," *Physics Letters A*, Vol. 434, 128036, 2022.

[6] Yin, B., Z. Xu, and Y. Ma, "Terahertz off-axis focus polarization converter based on metasurface," *Progress In Electromagnetics Research Letters*, Vol. 100, 91–97, 2021.

[7] Jiang, Y., L. Liu, S. Li, C. Tang, Z. Luo, Z. Zhu, Y. Cao, C. Gu, and Z. Li, "Highly efficient decoupled triple-channel OAM generation with a single-layer shared aperture reflective metasurface," *Advanced Optical Materials*, Vol. 11, No. 3, 2202071, 2023.

[8] Iyer, A. K., A. Alù, and A. Epstein, "Metamaterials and metasurfaces — Historical context, recent advances, and future directions," *IEEE Transactions on Antennas and Propagation*, Vol. 68, No. 3, 1223–1231, 2020.

[9] Sui, J.-Y., J.-H. Zou, S.-Y. Liao, B.-X. Li, and H.-F. Zhang, "High sensitivity multiscale and multitasking terahertz Janus sensor based on photonic spin Hall effect," *Applied Physics Letters*, Vol. 122, No. 23, 231105, 2023.

[10] Sui, J.-Y., S.-Y. Liao, B. Li, and H.-F. Zhang, "High sensitivity multitasking non-reciprocity sensor using the photonic spin hall effect," *Optics Letters*, Vol. 47, No. 23, 6065–6068, 2022.

[11] Sui, J.-Y., J.-H. Zou, S.-Y. Liao, B.-F. Wan, and H.-F. Zhang, "Short-wave infrared Janus metastructure with multitasking of wide-range pressure detection and high-resolution biosensing based on photonic spin Hall effect," *IEEE Transactions on Instrumentation and Measurement*, Vol. 73, 1–9, 2024.

[12] Ishfaq, M., X. Li, Z. Qi, W. Zhao, A. Aziz, L. Qiu, and S. Memon, "A transmissive metasurface generating wideband OAM vortex beam in the Ka-band," *IEEE Antennas and Wireless Propagation Letters*, Vol. 22, No. 8, 2007–2011, 2023.

[13] Ishfaq, M., X. Li, Z. Qi, W. Zhao, A. Aziz, and L. Qiu, "Wideband OAM vortex beam generation through a thin transmitarray in the Ka-band," *IEEE Antennas and Wireless Propagation Letters*, Vol. 23, No. 2, 688–692, 2024.

[14] Li, F., H. Chen, Y. Zhou, J. You, N. C. Panoiu, P. Zhou, and L. Deng, "Generation and focusing of orbital angular momentum based on polarized reflectarray at microwave frequency," *IEEE Transactions on Microwave Theory and Techniques*, Vol. 69, No. 3, 1829–1837, 2021.

[15] Jiang, L., S. Yu, and N. Kou, "Asymmetric transmission of OAM vortex waves by cylindrical Janus metasurface," *IEEE Antennas and Wireless Propagation Letters*, Vol. 22, No. 11, 2654–2658, 2023.

[16] Shahmirzadi, A. V., Z. Badamchi, B. Badamchi, and H. Subbaraman, "Generating concentrically embedded spatially divided OAM carrying vortex beams using transmitarrays," *IEEE Transactions on Antennas and Propagation*, Vol. 69, No. 12, 8436–8448, 2021.

[17] Duan, K., K. Chen, T. Jiang, J. Zhao, and Y. Feng, "Noninterleaved bidirectional metasurface for spatial energy allocation," *IEEE Transactions on Antennas and Propagation*, Vol. 72, No. 8, 6423–6436, 2024.

[18] Liu, S. L., X. Q. Lin, Y. H. Yan, and Y. L. Fan, "Generation of a high-gain bidirectional transmit-reflect-array antenna with asymmetric beams using sparse-array method," *IEEE Transactions on Antennas and Propagation*, Vol. 69, No. 9, 6087–6092, 2021.

[19] Wang, Y., Y. Ge, Z. Chen, X. Liu, J. Pu, K. Liu, H. Chen, and Y. Hao, "Broadband high-efficiency ultrathin metasurfaces with simultaneous independent control of transmission and reflection amplitudes and phases," *IEEE Transactions on Microwave Theory and Techniques*, Vol. 70, No. 1, 254–263, 2022.

[20] Lv, H.-H., Q.-L. Huang, X.-J. Yi, J.-Q. Hou, and X.-W. Shi, "Low-profile transmitting metasurface using single dielectric substrate for OAM generation," *IEEE Antennas and Wireless Propagation Letters*, Vol. 19, No. 5, 881–885, 2020.

[21] Guo, X. and Y. Yang, "Low-profile full-space transmission-reflection-integrated multiple focused and OAM beams metasurface for indoor communication," *IEEE Transactions on Microwave Theory and Techniques*, Vol. 73, No. 6, 3644–3654, 2025.

[22] Zheng, S., H. Hao, Y. Tang, and X. Ran, "High-purity orbital angular momentum vortex beam generator using an amplitude-and-phase metasurface," *Optics Letters*, Vol. 46, No. 23, 5790–5793, 2021.

[23] Xiong, Y., C. Xue, Q. Guo, T. Li, and X. Gao, "A shared-aperture transmissive/reflective bi-functional metasurface for both transmitarray and reflectarray," *AEU — International Journal of Electronics and Communications*, Vol. 164, 154631, 2023.

[24] Qin, Y., C. Xue, H. Shi, J. Yan, and X. Gao, "A double-layer metasurface-based dual-band dual-polarized transmit-reflect-array antenna," *IEEE Antennas and Wireless Propagation Letters*, Vol. 25, No. 4, 1567–1571, 2026.

[25] Yang, F., R. Deng, S. Xu, and M. Li, "Design and experiment of a near-zero-thickness high-gain transmit-reflect-array antenna using anisotropic metasurface," *IEEE Transactions on Antennas and Propagation*, Vol. 66, No. 6, 2853–2861, 2018.

[26] Guo, X., Y. Luo, N. Yan, W. An, and K. Ma, "Multi-beam transmit-reflect-array antenna using alternating transmission and reflection elements for space-air-ground-sea integrated network," *IEEE Transactions on Antennas and Propagation*, Vol. 71, No. 11, 8668–8676, 2023.